MICROBIOLOGY

# Upconversion dual-photosensitizer–expressing bacteria for near-infrared monochromatically excitable synergistic phototherapy

**Mian Chen[1,2], Qiuju Han[1,2], Mengmeng Zhang[1], Ying Liu[1], Lu Wang[1], Fengmin Yang[1], Qian Li[2]*, Zhenping Cao[1]*, Chunhai Fan[1,2], Jinyao Liu[1]***



**Synergistic phototherapy stands for superior treatment prospects than a single phototherapeutic modality. However, the combined photosensitizers often suffer from incompatible excitation mode, limited irradiation penetration depth, and lack of specificity. We describe the development of upconversion dual-photosensitizer–expressing bacteria (UDPB) for near-infrared monochromatically excitable combination phototherapy. UDPB are prepared by integrating genetic engineering and surface modification, in which bacteria are encoded to simultaneously express photothermal melanin and phototoxic KillerRed protein and the surface primary amino groups are derived to free thiols for biorthogonal conjugation of upconversion nanoparticles. UDPB exhibit a near-infrared monochromatic irradiation-mediated dual-activation characteristic as the photothermal conversion of melanin can be initiated directly, while the photodynamic effect of KillerRed can be stimulated indirectly by upconverted visible light emission. UDPB also show living features to colonize hypoxic lesion sites and inhibit pathogens via bacterial community competition. In two murine models of solid tumor and skin wound infection, UDPB separately induce robust antitumor response and a rapid wound healing effect.**

## INTRODUCTION

Phototherapies, such as photothermal therapy (PTT) and photodynamic therapy (PDT), have aroused tremendous interest due largely to their low invasiveness, high spatiotemporal controllability, minimal side effects, and the ability to avoid the occurrence of drug resistance (*1*–*3*). The development of advanced photosensitizers that are able to increase the efficiency of converting light energy into heat or promote the generation of reactive oxygen species (ROS) is critical for effective phototherapy (*4*, *5*). Despite a variety of elegant photosensitizers have been developed, the treatment efficacy by either PTT or PDT alone usually remains unsatisfactory (*6*). Combination of PTT and PDT can synergistically enhance treatment potency, emerging as a simple yet valid route to overcome the limitation of using an individual phototherapeutic modality (*7*–*9*). The main strategy to combine PTT and PDT is the integration of two different photosensitizers into a single system (*10*). Unfortunately, because of intrinsic photophysical properties, the combined photosensitizers often require two different excitation wavelengths, resulting in an incompatible system that needs multistep operation procedures (*11*–*13*). In addition, conventional photosensitizers along with their derivatives are always lack of specificity, particularly with respect to the complicated in vivo microenvironments, leading to insufficient therapeutic efficacy and even severe side effects (*14*). Therefore, approaches capable of synergizing phototherapies in a facile yet accurate and effective manner are highly desirable.

Bacteria have attracted increasing attention for various biomedical applications, benefiting from their natural characteristics, such as inherent motility, microbial community competition, hypoxia tropism, and preferential colonization (*15*–*18*). Another appealing feature of bacteria is that they are both chemically and genetically modifiable (*19*–*21*). By virtue of the presence of rich reactive groups on bacterial surfaces and the advancement of genetic engineering tools, the structure and function of bacteria can be feasibly modified, making them as emerging therapeutic candidates for disease treatment (*22*, *23*). In the past few years, bacteria have been frequently functionalized as vehicles to carry photosensitizers for PTT or PDT, with an aim to improve the accumulation in target site (*24*–*26*). However, bacteria simultaneously modified with two different photosensitizers to pursue synergistic phototherapy have been rarely reported (*27*). Meanwhile, previous methods especially via chemical modification are difficult to introduce bacteria with sufficient photosensitizers and the resultant bacteria-based combinations also inevitably suffer from incompatible excitation mode (*28*, *29*). The inadequate penetration depths of ultraviolet and visible lights render it challenging to obtain optimal treatment efficacy for bacteria-based synergistic phototherapy (*30*, *31*). Thus, it is imperative to explore how the living characteristics of bacteria and the benefits of synergistic phototherapy can be easily combined to achieve superior therapeutic outcomes.

Here, the development of upconversion dual-photosensitizer–expressing bacteria (UDPB) is reported for near-infrared (NIR) monochromatically excitable synergistic PTT and PDT (Fig. 1). By integrating synthetic bioengineering and surface modification, bacteria are genetically encoded to dually express biogenic photothermal melanin and photosensitive KillerRed fluorescence protein, while the primary amino moieties on bacterial surface are modified to thiol groups via imidoester reaction for thiol-mediated click conjugation of upconversion nanoparticles (UCNPs). The resulting UDPB show a unique monochromatic irradiation-enabled dual-activation mode. Namely, the photothermal conversion of melanin can be stimulated directly by NIR irradiation, which can also be upconverted to visible light emission to activate the photodynamic effect of KillerRed. UDPB present natural superiorities in synergistic phototherapy by means of

[1]Shanghai Key Laboratory for Nucleic Acid Chemistry and Nanomedicine, Institute of Molecular Medicine, State Key Laboratory of Systems Medicine for Cancer, Renji Hospital, School of Medicine, Shanghai Jiao Tong University, Shanghai 200127, China. [2]School of Chemistry and Chemical Engineering, Frontiers Science Center for Transformative Molecules and National Center for Translational Medicine, Shanghai Jiao Tong University, Shanghai 200240, China.
*Corresponding author. Email: jyliu@sjtu.edu.cn (J.L.); caozhenping@renji.com (Z.C.); liqian2018@sjtu.edu.cn (Q.L.)

their living characteristics that can colonize hypoxic lesion tissues and resist pathogens through bacterial community inhibition. In two mouse models of breast tumor and *Staphylococcus aureus* (*S. aureus*) infection of skin wound, UDPB demonstrate satisfactory therapeutic potentials through producing adequate local hyperthermia and ROS level in the lesion sites. Specifically, UDPB elicit a potent antitumor response by triggering a systemic immune response and causing apoptosis of tumor cells. UDPB also generate an accelerated healing effect of chronic wound infection by destructing the outer membrane of *S. aureus* and suppressing the overactivated inflammatory responses. We anticipate that UDPB can inspire the preparation of advanced photosensitizers and provide a unique strategy for synergizing different phototherapies for disease treatment.

## RESULTS

### Preparation and characterization of UDPB

To introduce bacteria with both PTT and PDT effects, we used genetic engineering to construct and transform plasmids carrying both *tyrosinase* gene and *KillerRed* gene into a model strain of BL21 (Bac), enabling dual production of melanin and KillerRed. It is worth mentioning that melanin has a stable and high photothermal conversion efficiency under 808-nm NIR irradiation and is a widely used biological photosensitizer with excellent biocompatibility (*32*, *33*). KillerRed is a phototoxic red fluorescent protein that can generate biotoxic ROS under visible light irradiation (*34*, *35*). To validate the successful construction of engineered bacteria-producing melanin and KillerRed (Bac-MK), DNA gel electrophoresis of colony polymerase chain reaction (PCR) was performed and the image shown in fig. S1 demonstrated that Bac-MK exhibited two bands at the expected sizes of *tyrosinase* and *KillerRed*. We also observed that the colonies turned black on agar plate and emitted red fluorescence (FL) after excitation, indicating the dual-production of melanin and KillerRed in Bac-MK (Fig. 2A). As shown in fig. S2, bacteria-expressing tyrosinase only produced melanin (Bac-M) and turned black on the plate, but showed ignorable FL emission under irradiation. While bacteria-expressing KillerRed (Bac-K) appeared light yellow on the plate and displayed an intensive red FL signal upon excitation. FL spectra illustrated that Bac-MK could be excited at 582 nm (Fig. 2B), which was far below the excitation of melanin at 808 nm. Namely, there was a mismatch in the excitation spectra of melanin and KillerRed. To enable a monochromatic irradiation-mediated dual-activation mode,

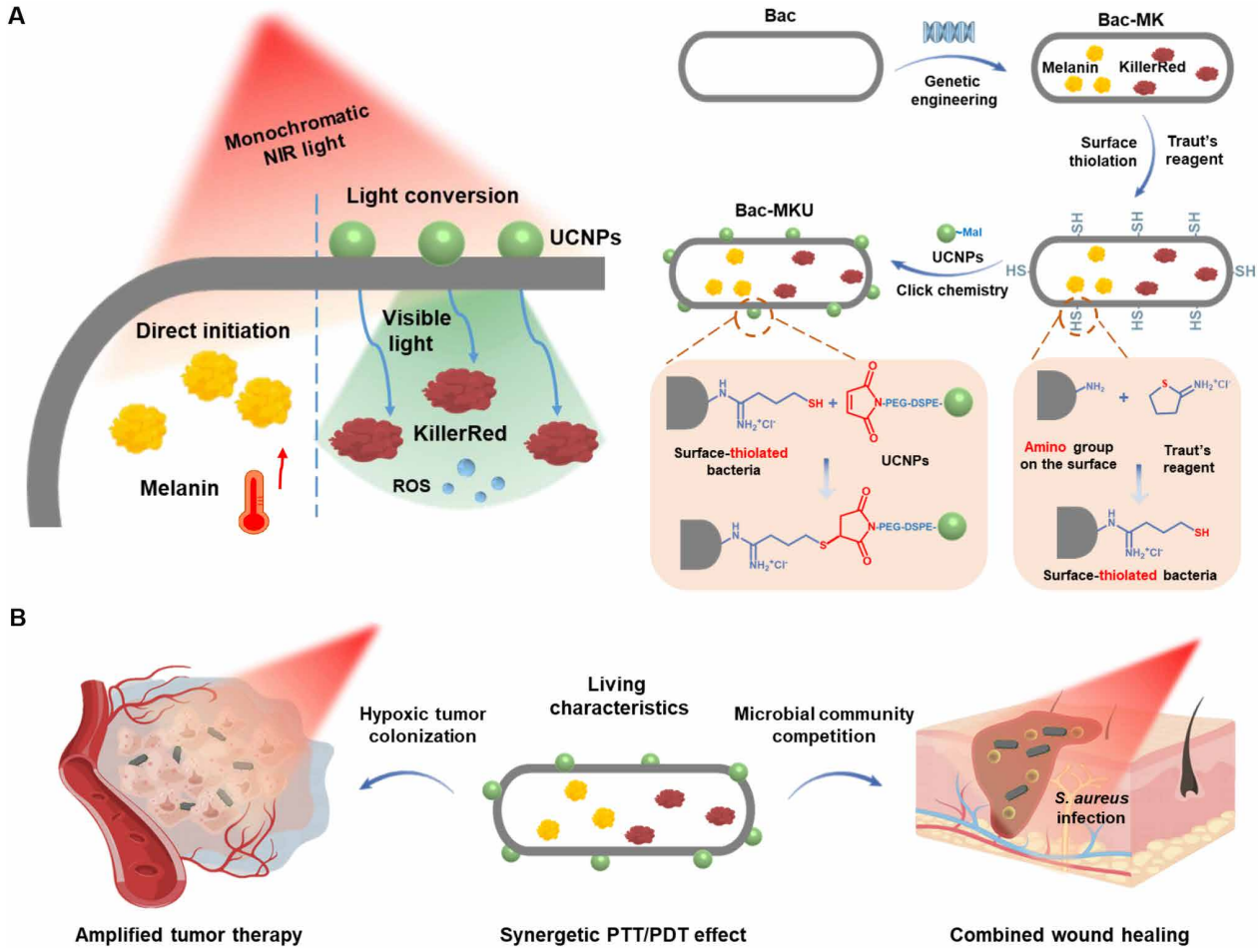


**Fig. 1. Schematic illustration.** (**A**) Synthesis of UDPB for NIR monochromatically excitable synergistic phototherapy. (**B**) Advantages of UDPB in amplifying antitumor effect and accelerating the healing of wound infection. PTT, photothermal therapy; PDT, photodynamic therapy; UCNPs, upconversion nanoparticles; ROS, reactive oxygen species.

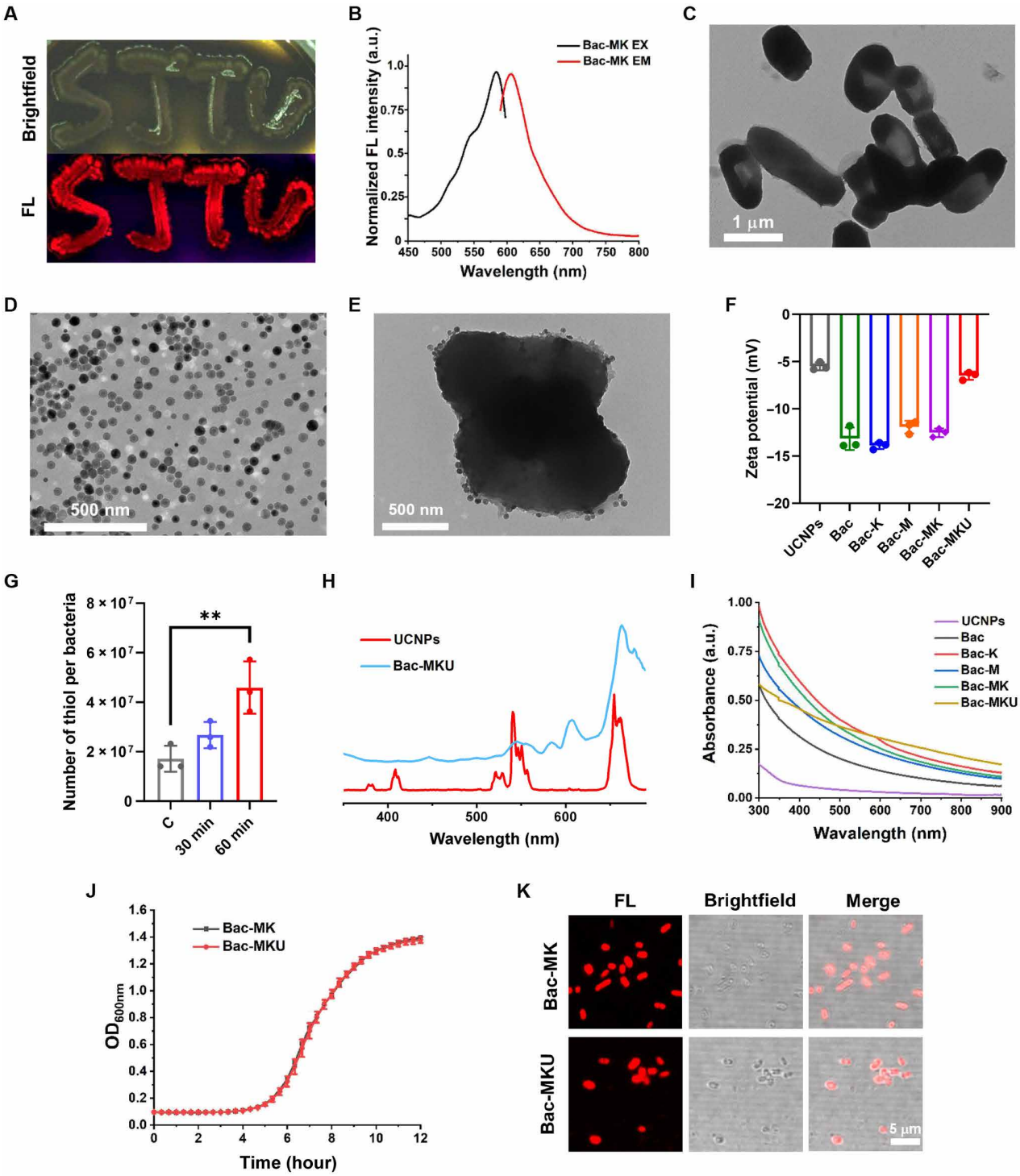


**Fig. 2. Characterization of UDPB.** (**A**) Coexpression of melanin (brightfield) and KillerRed [fluorescence (FL)] in Bac-MK displaying on plate. (**B**) Photoluminescence spectra of Bac-MK. (**C**) Typical TEM image of Bac-MK. (**D**) and (**E**) Typical transmission electron microscopy (TEM) images of Er@Yb@Nd@Y UCNPs and Bac-MKU. (**F**) Zeta potential measured by dynamic light scattering. Data were presented as means ± SD ($n = 3$). (**G**) Number of thiol groups on each bacterial cell after treatment with Traut's reagent for 30 and 60 min, respectively. Bacteria without Traut's reagent treatment were used as a control. Data were presented as means ± SD ($n = 3$). (**H**) Photoluminescence spectra of UCNPs and Bac-MKU under 808-nm excitation. (**I**) Ultraviolet-visible spectra of UCNPs and different bacteria. (**J**) Optical density at 600 nm ($OD_{600nm}$) values of Bac-MK and Bac-MKU after modification with UCNPs. (**K**) Confocal images of Bac-MK and Bac-MKU. Significance was analyzed by one-way analysis of variance (ANOVA) with Tukey's post-test. a.u., arbitrary units. $^{**}P < 0.01$.

we designed UDPB, a hybrid bacteria-UCNPs system, by covalently attaching UCNPs onto the surface of Bac-MK. According to previous reports (*36*, *37*), $NaYF_4$:Yb,Er@$NaYF_4$:Yb@$NaNdF_4$:Yb@$NaYF_4$:Yb (Er@Yb@Nd@Y) UCNPs were prepared via thermal decomposition, followed by introducing maleimide groups onto the surface using an ultrasound-assisted thin-film hydration approach. Meanwhile, the primary amino groups on the surface of Bac-MK were converted to thiol moieties with the help of a Traut's reagent (*38*, *39*), allowing the covalent conjugation of UCNPs by thiol-mediated click chemistry.

Typical transmission electron microscopy (TEM) images showed that the morphology of UCNP-decorated Bac-MK (Bac-MKU) was rod-shaped with a size of 1 to 2 μm (Fig. 2C), and Er@Yb@Nd@Y UCNPs appeared as spherical nanoparticles with an average diameter of ~41 nm and a relatively small size distribution (Fig. 2D and fig. S3). Clearly, a large number of UCNPs were anchored onto the surface of Bac-MKU after conjugation (Fig. 2E). To prove the attachment of UCNPs via thiol-mediated click chemistry, we mixed unthiolated bacteria with UCNPs and found that only a few particles attached onto the surface of bacteria (fig. S4). Dynamic light scattering (DLS) measurement indicated that the surface charges of both UCNPs and bacteria were negative, suggesting that the attachment of UCNPs onto Bac-MKU was mainly attributed to thiol-mediated click chemistry rather than electrostatic adsorption (Fig. 2F). The thiolation level of bacteria was analyzed after reacting with Traut's reagent for different times and showed a positive correlation with reaction time. After reaction for 1 hour, the thiol level of Bac-MKU was over twice higher than that of the untreated group (Fig. 2G). TEM images showed limited variation on bacterial morphology after Traut's reagent treatment (fig. S5). To determine the amount of UCNPs on Bac-MKU, we measured the neodymium content by inductively coupled plasma–mass spectrometry. It showed that the loading of UCNPs on the thiolated bacteria reached 5.47 μg per optical density (OD) of bacteria, whereas the use of unthiolated bacteria yielded only 0.53 μg per OD of bacteria, further verifying that surface thiolation could effectively facilitate the decoration of UCNPs by click chemistry. Photoluminescence spectra indicated that the emission peaks of UCNPs upon 808-nm irradiation were in the range of 516 to 560 nm, which well covered the maximum absorption of KillerRed (Fig. 2H). The peak intensity emitted at ~545 nm was notably weakened, implying that the phototransformation of UCNPs occurred on bacteria. Ultraviolet-visible (UV-Vis) spectra depicted that the absorbances of Bac-MKU were different from other types of bacteria, attributing to the conjugation of UCNPs (Fig. 2I). To investigate the influence of UCNPs on bacterial growth, the growth curves of Bac-MK and Bac-MKU at $OD_{600nm}$ were recorded, respectively. As plotted in Fig. 2J, the similar growth profiles demonstrated the negligible effect of surface modification on bacterial activity. Moreover, the growth curves of Bac, Bac-M, and Bac-K at $OD_{600nm}$ suggested that these bacteria had a similar growth pattern (fig. S6). Comparable to Bac-MK, Bac-MKU presented bright red fluorescence under confocal laser scanning microscopy (CLSM) imaging, certifying the limited influence of UCNP attachment on the fluorescence properties of the modified bacteria (Fig. 2K).

### In vitro photothermal and photodynamic effects of UDPB

We systematically analyzed the photothermal and photodynamic effects of Bac-MKU in vitro. The temperature variations of Bac-MKU under NIR 808-nm irradiation at different laser powers were recorded. As the laser intensity rising from 0.8 to 1.2 W $cm^{-2}$, the temperature remarkably increased by 10°C to over 30°C after exposing $3 \times 10^8$ colony forming units (CFU) $ml^{-1}$ of bacteria for 180 s (Fig. 3, A and B). As controls, the performances of phosphate-buffered saline (PBS), Bac, Bac-K, Bac-M, and Bac-MK were measured at a laser power of 1.0 W $cm^{-2}$ (Fig. 3C). In contrast to PBS, Bac, and Bac-K that presented negligible changes, the temperature of melanin-expressing bacteria including Bac-M and Bac-MK could reach ~46°C upon exposure for 180 s, exhibiting a rising trend similar to Bac-MKU (Fig. 3D). After undergoing four cycles of photothermal treatment, the temperature-rising ability of Bac-MKU remained near unchanged, suggesting the potential for repeated light irradiation (Fig. 3E). We next used the light conversion ability of UCNPs to induce the ROS generation of Bac-MKU under NIR 808-nm irradiation. By using 2,7-dichlorodihydrofluorescein diacetate (DCFH-DA), a commercial ROS indicator that could be oxidized by ROS to emit a green fluorescence signal (*40*, *41*), Bac-MKU exhibited a notable improvement in ROS generation compared to all the control groups, which was simply ascribed to the presence of UCNPs (Fig. 3F). It was worth noting that irradiation durations had a distinct influence on bacterial activity (Fig. 3G). The growth curves at $OD_{600nm}$ over different irradiation durations suggested that Bac-MKU remained a relatively preferable bacterial activity after 5-min irradiation, while the bacteria were almost inactivated with irradiation time extending to 10 or 15 min.

We further measured the photothermal and photodynamic properties of Bac-MKU after co-incubation with different cells. Both eukaryotic and prokaryotic cell models were used for this study. As displayed in fig. S7, all of the 4T1 cells treated with $3 \times 10^8$ CFU $ml^{-1}$ of melanin-producing bacteria including Bac-M, Bac-MK, and Bac-MKU emerged an obvious temperature rising trend compared to the PBS and Bac-K groups, which was attributed to the photothermal effect of melanin. After exposure to laser irradiation for 3 min, the temperature of these cells treated with melanin-producing bacteria could reach up to 46°C (fig. S7), verifying a robust photothermal effect. To study the photodynamic effect of Bac-MKU, we measured the generation of ROS in 4T1 cells by using DCFH-DA. Cells were treated with $3 \times 10^8$ CFU $ml^{-1}$ of Bac-MKU and irradiated with 808-nm NIR light for 1 min. Typical CLSM images in Fig. 3I showed that the bright green fluorescence representing ROS was only observed in cells treated with Bac-MKU, while there was almost no fluorescence signal generated in cells treated with other bacteria. It claimed that the Bac-MKU cell group produced ROS, and the photodynamic effect of KillerRed could be triggered by NIR irradiation only after modifying with UCNPs. We also evaluated the effects of PTT and PDT on cells produced by Bac-MKU at different concentrations. As bacterial concentration increased, the photothermal temperature gradually elevated, accompanied by an increase in the production of ROS (fig. S8). Similarly, the temperatures of prokaryotic *S. aureus* cells separately treated with Bac-M, Bac-MK, and Bac-MKU could reach up to 46°C after 3-min irradiation, which was consistent with the temperature rise of 4T1 cells (fig. S9). The generation of ROS in *S. aureus* cells treated with Bac-MKU also exhibited a significant improvement compared to all the control groups after irradiation, further demonstrating the satisfied photothermal and photodynamic effects in vitro (Fig. 3H). Together, Bac-MKU could be dually activated to raise local temperature and generate ROS under NIR exposure, confirming that the proposed monochromatic irradiation-mediated dual-activation mode was successfully achieved by combining UCNPs with melanin and KillerRed. To investigate the retention of UCNPs on the surface of bacteria over time, the ROS fluorescence signal ratio of Bac-MKU to Bac-MK was compared at different time points by incubation in PBS or Dulbecco's

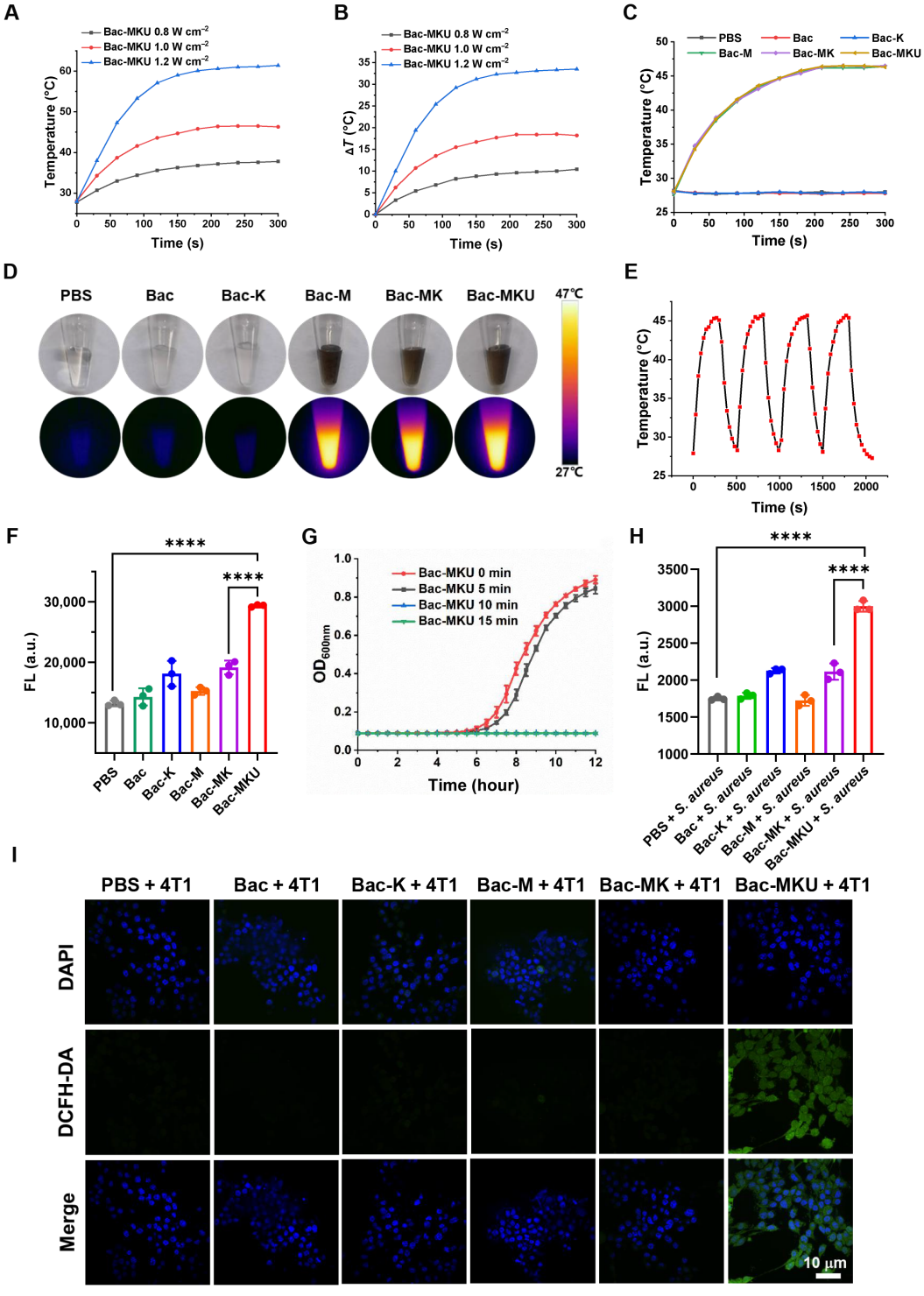


**Fig. 3. In vitro photothermal and photodynamic effects of UDPB.** (**A**) Temperature rises and (**B**) variations of Bac-MKU under 808-nm NIR light irradiation at different laser powers. (**C**) Temperature rises of Bac, Bac-K, Bac-M, Bac-MK, and Bac-MKU under NIR light irradiation at the power of 1.0 W $cm^{-2}$. PBS was used as a control. (**D**) Digital and thermal imaging of different groups under NIR light irradiation. (**E**) Photothermal effects of Bac-MKU at the power of 1.0 W $cm^{-2}$ during four cycles of irradiation. (**F**) ROS generation of different bacterial groups under NIR light irradiation for 1 min detected by the fluorescence of DCFH-DA. PBS was used as a control. Data were presented as means ± SD ($n = 3$). (**G**) $OD_{600nm}$ value of Bac-MKU after treatment with different durations of light irradiation. Data were presented as means ± SD ($n = 3$). (**H**) Fluorescence intensity representing ROS generation in *S. aureus* cells after treatment with different bacterial groups under NIR light irradiation for 1 min. *S. aureus* cells treated with PBS were as a control. Data were presented as means ± SD ($n = 3$). (**I**) Fluorescence signal representing ROS inside 4T1 tumor cells from different groups after 1-min NIR light irradiation. 4T1 tumor cells treated with PBS were as a control. Cell nuclei were stained with 4′,6-diamidino-2-phenylindole (DAPI). Data were presented as means ± SD. Significance was analyzed by one-way ANOVA with Tukey's post-test. ****$P < 0.0001$.

modified Eagle's medium (DMEM) supplemented with fetal bovine serum (FBS) (fig. S10). The fluorescence ratio of ROS decreased over time in the culture medium but remained around 130% after 8-hour incubation. While, the fluorescence ratio displayed minimal change in PBS, suggesting that the retention was relatively long-lasting on bacteria. Moreover, TEM images captured after 8-hour incubation provided a visual confirmation of the presence of UCNPs on the bacterial surface.

### In vivo photothermal and photodynamic effects of UDPB

The photothermal and photodynamic effects of Bac-MKU were further measured in vivo. We first developed a mouse model of subcutaneous 4T1 breast tumor to assess the productions of local hyperthermia and ROS. The temperature of tumor after treating mice with $3 \times 10^7$ CFU bacteria was recorded under NIR 808-nm irradiation for 300 s. The tumor temperatures of the Bac-M, Bac-MK, and Bac-MKU groups reached up to 45°C rapidly, which was consistent with the in vitro results (Fig. 4, A and C). It was worth highlighting that the use of Bac-MKU could be expected to conduct PTT at a moderate temperature to effectively diminish unwanted damage to surrounding normal tissues (*42*). Differently, the variations of tumor temperature in the PBS, Bac, and Bac-K groups were limited. We also detected the in vivo generation of ROS to investigate the PDT potential inside tumor tissue. Because of the short lifetime of the generated ROS, the tumor tissue was immediately sectioned after NIR irradiation and prepared for frozen sections (*43*, *44*). As expected, compared to the PBS and Bac-MK groups, Bac-MKU treatment exhibited strong green fluorescence, which was attributed to the oxidation of DCFH-DA by ROS produced within the tumor (Fig. 4E). These results validated that Bac-MKU could effectively perform photothermal and photodynamic effects in tumor tissue under monochromatic NIR irradiation. We developed a mouse model of skin wound to further study the in vivo performance of Bac-MKU. The temperature rise of the wound surface under irradiation was monitored after treating with $3 \times 10^7$ CFU bacteria. The temperature curves revealed that similar to Bac-MK, Bac-MKU could quickly reach a temperature of ~45°C on the wound surface after a short period of 3-min exposure to NIR 808-nm laser, which was consistent with the temperature rise in the tumor model (Fig. 4, B and D). The wound tissue was also sampled for frozen sections to assess the photodynamic effect. Similarly, Bac-MKU treatment exhibited strong green fluorescence, indicating the production of abundant ROS in the skin wound (Fig. 4F). The results showed that Bac-MKU could produce an excellent in vivo photothermal and photodynamic effect in both mouse models of tumor and skin wound.

### Living characteristics of UDPB

As living bioagents, bacteria have been reported to be able to preferentially colonize hypoxic, nutrient-rich, and immunosuppressive tumor tissue (*15*, *21*). To investigate the distribution and penetration of Bac-MKU inside the tumor, we first established an in vitro tumor spheroid model (*45*). After co-incubation with $3 \times 10^8$ CFU $ml^{-1}$ bacteria for 4 hours, the innate fluorescence signals of KillerRed associated with Bac-MKU were detected conformably at both the internal space and edge of the tumor spheroid, suggesting that Bac-MKU could penetrate deeply and distribute evenly inside tumor (Fig. 5A). We further studied the biodistribution of Bac-MKU in 4T1 breast tumor–bearing mice. At 5 days after administration of $3 \times 10^7$ CFU bacteria, the samples of tumor tissue, blood, and major organs including the heart, liver, spleen, lung, and kidney were collected for bacterial plate counting. As shown in Fig. 5 (B and C), almost all bacteria in the Bac-MKU group accumulated inside the tumor, whereas none or negligible quantities of bacteria were presented in normal organs. It was noted that there was no notable difference in intratumoral bacterial number between the Bac-MK and Bac-MKU groups, reflecting that decoration with UCNPs had no negative influence on bacterial mobility and residence in tumor tissue. Besides, the overall intratumoral penetration and distribution of Bac-MKU could be observed directly by capturing the fluorescence signal of KillerRed using CLSM. The frozen sections of tumor tissue sampled at 8-hour after injection showed obvious red fluorescence throughout the entire tumor, ranging from inner core to the edge region (Fig. 5D). The uniform distribution of Bac-MKU inside tumor tissue could be beneficial to amplify the efficacy of phototherapy.

In addition to tumor colonization preference, bacteria are capable to combat pathogens through microbial community inhibition (*18*, *22*, *46*). As a type of pathogen commonly found on the skin, *S. aureus* is the leading cause of skin wound infection (*47*). We cocultured Bac-MKU with *S. aureus* to evaluate their community competition. Encouragingly, despite that a negligible antibacterial effect of Bac toward *S. aureus* was detected at a low feed ratio of 1:10 (Bac to *S. aureus*), increased feed ratios of both 1:1 and 10:1 showed apparent inhibition efficacy (fig. S11A). Under non-illuminated conditions, both Bac-MK and Bac-MKU presented enhanced ability to inhibit the growths of *S. aureus* at different feed ratios (Fig. 5, E and F). Even at the low feed ratio of 1:10 (Bac-MK/Bac-MKU to *S. aureus*), co-incubation with either Bac-MK or Bac-MKU could efficiently suppress the proliferation of *S. aureus*. Plate counting clarified that with the feed ratio increasing to 10:1, higher than 80% of *S. aureus* were inhibited by Bac-MKU. After co-incubation with *S. aureus*, the growths of Bac-MK and Bac-MKU were not affected as comparable numbers were found to that of untreated bacteria (Fig. 5, G and H). It was worth pointing out that the growths of Bac were significantly suppressed after coculture with *S. aureus* (fig. S11B). Particularly, with feed ratios decreasing to 1:1 or 1:10, higher than 55% of Bac were suppressed. We speculated that the intracellular accumulations of melanin and KillerRed were the sources behind the antibacterial effects against *S. aureus*.

### Advantages of UDPB in tumor therapy

Encouraged by the combined photothermal and photodynamic effects as well as the living characteristics to colonize tumor site, we examined the therapeutic value of Bac-MKU for tumor treatment. First, the in vitro synergistic cytotoxicity of Bac-MKU under NIR 808-nm irradiation was determined by directly co-incubating with 4T1 cells. Flow cytometry–based cell apoptotic analysis was conducted by staining with annexin V–fluorescein isothiocyanate (FITC)/propidium iodide (PI) (*48*, *49*). Expectedly, only a small portion of 4T1 cells underwent apoptosis in the PBS, Bac, and Bac-K groups after NIR exposure, indicating that most of the cells remained alive (Fig. 6A). Benefiting from the photothermal effect of melanin, cells treated with Bac-M and Bac-MK separately showed 17.6 and 19.5% of cell apoptosis. Notably, the apoptotic rate of Bac-MKU–treated cells increased up to 66.5% due to the synergistic effect of PTT and PDT (Fig. 6B). We further evaluated the antitumor efficacy of Bac-MKU in the 4T1 cell–based three-dimensional tumor spheroid model (Fig. 6C). The tumor spheroids without bacterial treatments could maintain the spherical shape after light exposure, while the ones treated with Bac-MK were ruptured apparently. Differently, the spheroids treated with

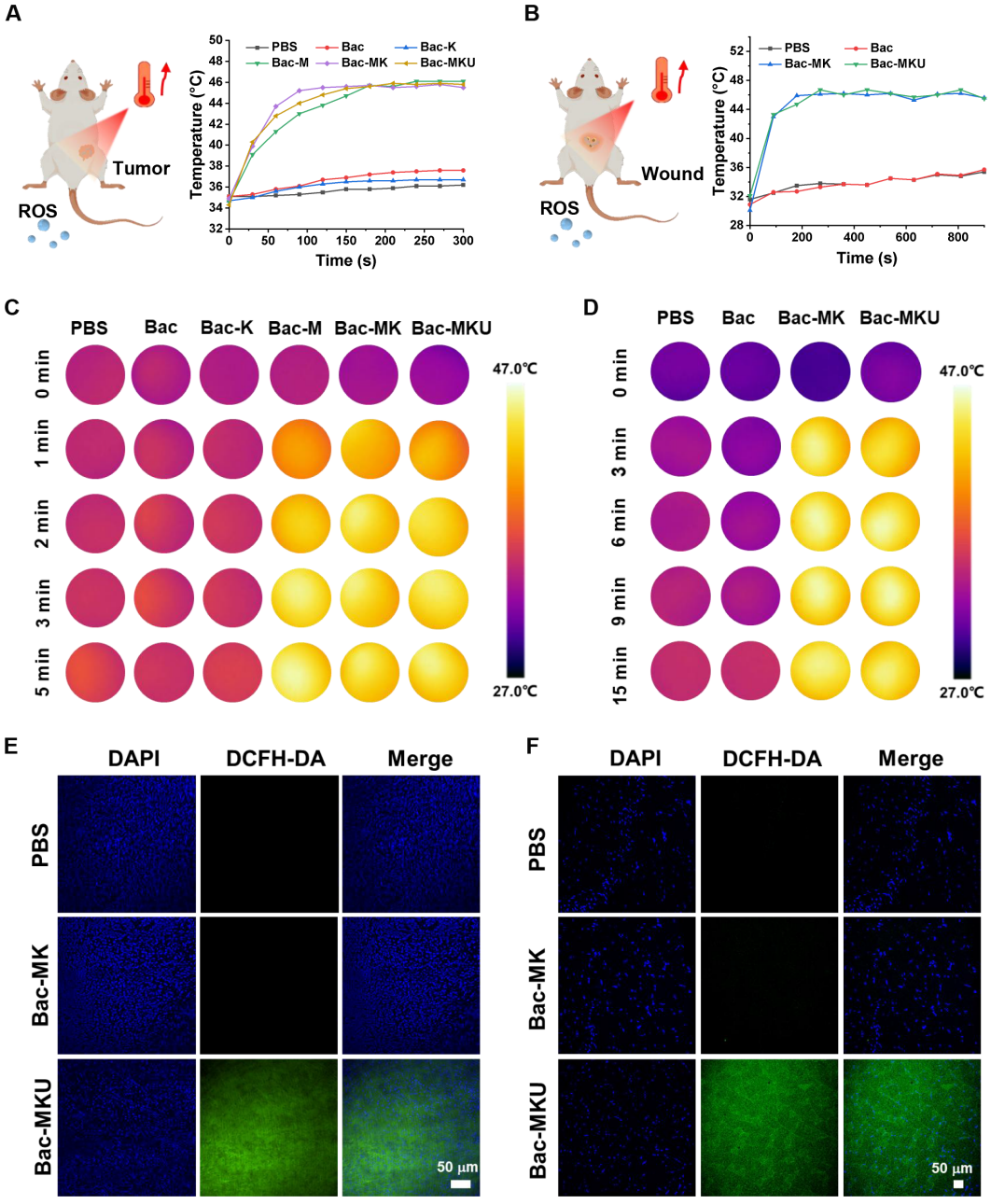


**Fig. 4. In vivo photothermal and photodynamic effects of UDPB.** Temperature rises of (**A**) tumor and (**B**) skin wound tissues in mouse models of breast tumor and *S. aureus* infection of skin wound after treatment with Bac, Bac-K, Bac-M, Bac-MK, or Bac-MKU at a dose of $3 \times 10^8$ CFU $ml^{-1}$ under 808-nm NIR light irradiation for 5 and 15 min, respectively. Corresponding tissues treated with PBS were as a control. To visualize in vivo temperature variation after exposure to NIR light, thermal images at 0, 1, 2, 3, and 5 min in (**C**) 4T1 tumor and at 0, 3, 6, 9, and 15 min in (**D**) skin wound tissues after corresponding treatments were recorded in a temperature-rising process. To determine in vivo ROS generation, ROS levels in (**E**) 4T1 tumor and (**F**) skin wound tissues were detected after Bac-MK or Bac-MKU treatment under 808-nm NIR light irradiation for 5 and 15 min, respectively. Corresponding tissues treated with PBS were as a control. Cell nuclei were stained with DAPI.

Bac-MKU were destructed into debris completely, implying that Bac-MKU–mediated combination of PTT and PDT was far superior to a single therapy modality. We also assessed the in vivo therapeutic value of Bac-MKU in subcutaneous 4T1 tumor-bearing mice, which were characterized by a low immune response and poor immunogenicity (*50*). Experimental design of the treatment was described in Fig. 6D. It was found that the tumors in the PBS, Bac, and Bac-K groups grew continuously with no apparent difference among them (Fig. 6E). Because of the photothermal property of melanin, single PTT mediated by Bac-M or Bac-MK exhibited an effective tumor-growth inhibition. While compared to all the control groups, Bac-MKU displayed the best antitumor efficacy, as supported by the slowest tumor growth and the lowest weight of the collected tumors (Fig. 6F and figs. S12 and S13). The enhanced treatment efficacy could

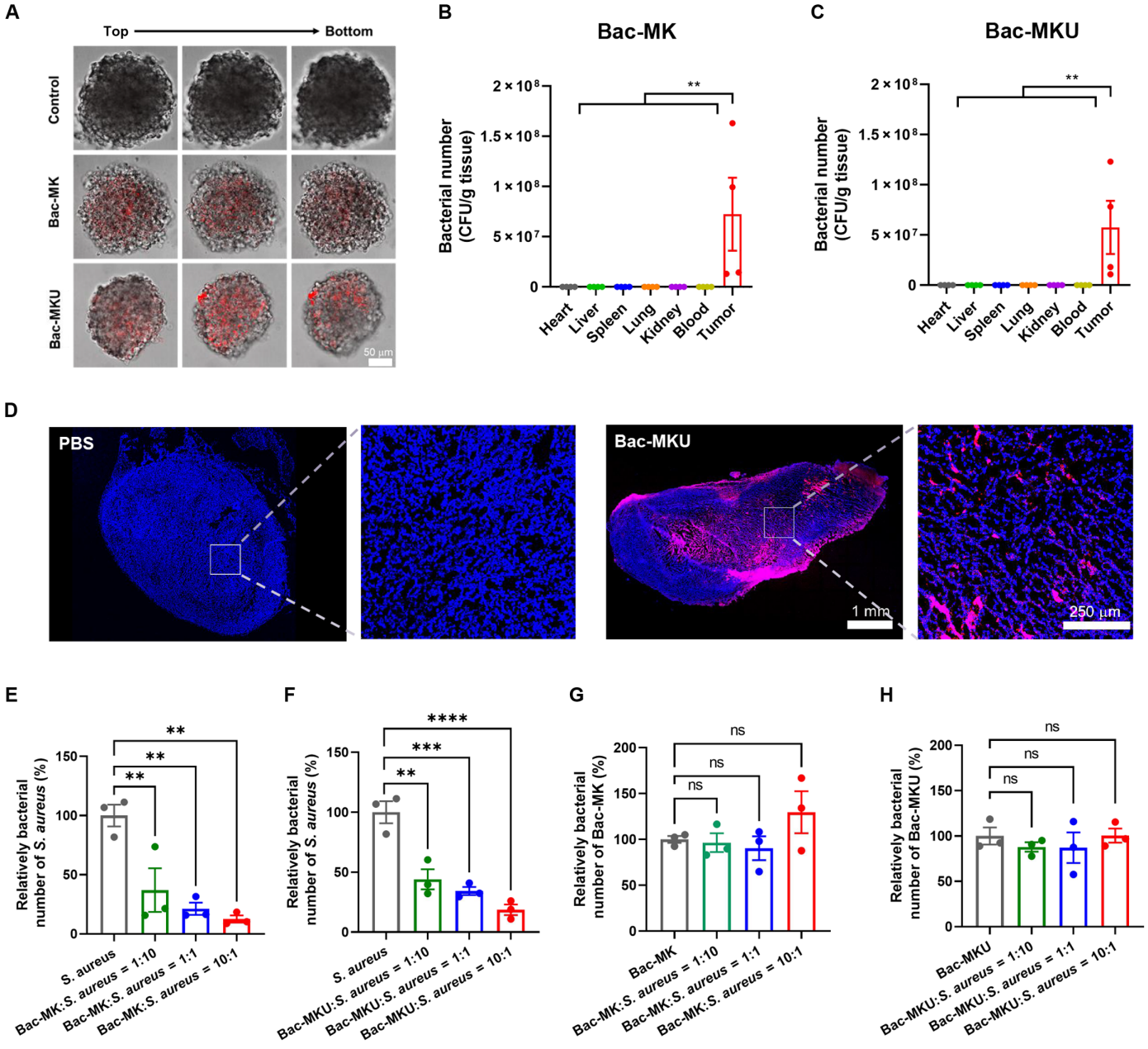


**Fig. 5. Living characteristics of UDPB.** (**A**) Confocal images displaying the distribution of fluorescent Bac-MK and Bac-MKU in 4T1 tumor spheroids (20 μm per step). 4T1 tumor spheroids treated with PBS were as a control. Biodistributions of (**B**) Bac-MK and (**C**) Bac-MKU in major organs, blood, and tumor determined by plate counting. Data were presented as means ± SD ($n = 4$). (**D**) Fluorescence images presenting the intratumoral distribution of Bac-MKU at 8 hours by ice-cutting 4T1 subcutaneous tumors. PBS-treated group was used as a control. Cell nuclei were stained with DAPI. Number of *S. aureus* after competing with (**E**) Bac-MK or (**F**) Bac-MKU under different feed ratios. The obtained bacterial number/the bacterial number in the corresponding control groups represented relatively bacterial number of *S. aureus*. Data were presented as means ± SD ($n = 3$). Relatively bacterial number of (**G**) Bac-MK or (**H**) Bac-MKU after competing with *S. aureus* under different feed ratios. Data were presented as means ± SD ($n = 3$). Significance was analyzed by one-way ANOVA with Tukey's post-test. $^{**}P < 0.01$, $^{***}P < 0.001$, and $^{****}P < 0.0001$. ns, no significance.

be simply attributed to the synergistic effect of PPT and PDT. In addition, compared to the PBS group, no obvious fluctuation in body weight was observed among all treated groups, suggesting limited side effects caused during treatment (fig. S14). Hematoxylin and eosin (H&E) staining of major organs harvested from treated mice demonstrated favorable biosafety of these living phototherapeutic bioagents as no detectable pathological changes were occurred (fig. S15).

To disclose the underlying antitumor mechanism, we analyzed both immune responses and apoptosis of tumor cells caused by Bac-MKU–mediated synergistic phototherapy. Both tumor-draining lymph nodes (TDLNs) and spleen tissues were collected at day 5 after treatment for flow cytometry and immunofluorescence measurements. As plotted in Fig. 6G and fig. S16, the expressions of CD80, CD86, CD11c, and major histocompatibility complex–II (MHC-II)

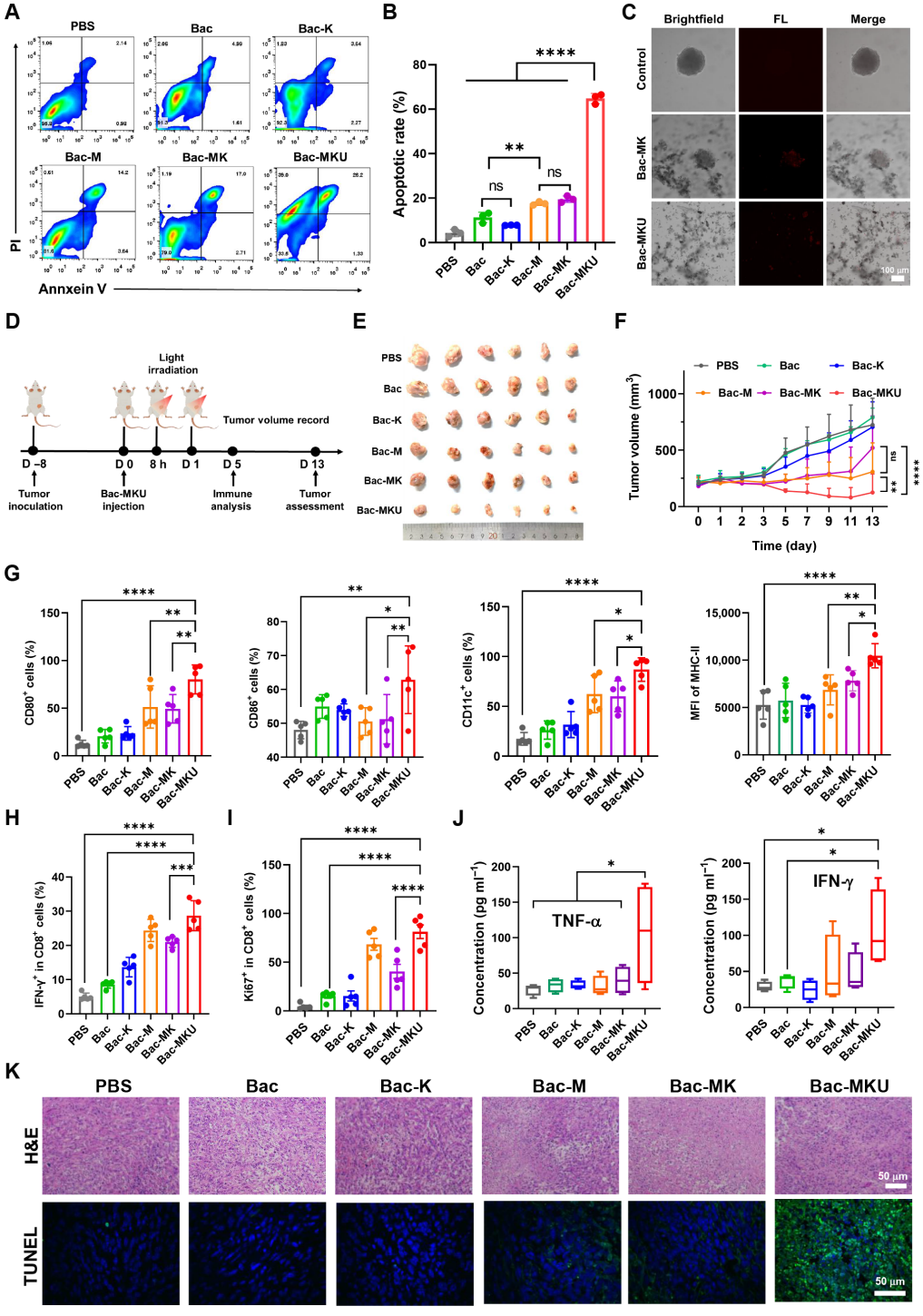


**Fig. 6. Advantages of UDPB in tumor therapy.** (**A**) Flow cytometric analysis and (**B**) statistical quantification of 4T1 tumor cell apoptosis in different treatment groups after NIR light irradiation. 4T1 tumor cells treated with PBS were used as a control. Data were presented as means ± SD ($n = 3$). (**C**) Confocal images of 4T1 tumor spheroids in the Bac-MK and Bac-MKU groups after NIR light irradiation. 4T1 tumor spheroids treated with PBS were used as a control. (**D**) Experimental design for assessing therapeutic efficacy. (**E**) Photograph of tumors sampled from different treatment groups at day (D) 13. (**F**) Tumor growth after different treatments during the therapeutic periods. Data were presented as means ± SD ($n = 6$). (**G**) Flow cytometric analysis of $CD80^+$, $CD86^+$, $CD11c^+$, and MHC-II DC cells in tumor-draining lymph nodes (TDLNs) collected from mice at day 5 after different treatments. Data were presented as means ± SD ($n = 5$). Flow cytometric analysis of the percentages of (**H**) IFN-$\gamma^+$ and (**I**) $Ki67^+$ in $CD8^+$ cells in TDLNs collected from mice at day 5 after different treatments. Data were presented as means ± SD ($n = 5$). (**J**) Qualification of TNF-α and IFN-γ in serum of 4T1 tumor-bearing mice at day 5 after different treatments. Data were presented as means ± SD ($n = 4$). (**K**) Hematoxylin and eosin (H&E) and TUNEL staining of 4T1 tumor tissues collected from mice at day 13 after different treatments. Cell nuclei were stained with DAPI. Significance was analyzed by one-way or two-way ANOVA with Tukey's post-test. $^*P < 0.05$, $^{**}P < 0.01$, $^{***}P < 0.001$, and $^{****}P < 0.0001$. ns, not significant.

on dendritic cells (DCs) in both TDLNs and spleen tissues sectioned from mice treated with Bac-MKU were significantly higher than those in all control groups, indicating the maturation of DCs by capturing tumor antigens (*51*). We further evaluated whether the synergistic phototherapy triggered a T cell response (Fig. 6, H and I, and fig. S17). The expression levels of $Ki67^+$ in TDLNs and the spleen were considerably increased in the Bac-MKU group compared to all other groups, testifying significant promotion of T cell proliferation (*52*). As interferon-γ (IFN-γ) is mainly produced by activated natural killer cells, Th1 cells, and $CD8^+$ cytotoxic cells (*53*), the enhanced proportion of IFN-γ further disclosed that Bac-MKU treatment could upregulate IFN-γ–mediated immune responses. We also found that the levels of tumor necrosis factor–α (TNF-α), IFN-γ, interleukin-1β (IL-1β), and IL-6 in mouse serum samples after treatment with Bac-MKU were higher than those in the rest groups (Fig. 6J and fig. S18). These results verified that Bac-MKU–mediated synergistic phototherapy could elicit a systemic immune response by promoting DC maturation and T cell proliferation. To validate the apoptosis of tumor cells, we carried out a histopathological examination of the collected tumors by using H&E and terminal deoxynucleotidyl transferase–mediated deoxyuridine triphosphate nick end labeling (TUNEL) staining (Fig. 6K). H&E staining revealed that in the Bac-MKU group, tumor cell nuclei were markedly fragmented and reduced in size. Consistently, compared to other groups, TUNEL staining showed that Bac-MKU–mediated phototherapy effectively promoted the apoptosis and proliferation inhibition of tumor cells, as revealed by intracellular FITC labeling of damaged DNA (*54*).

**Superiorities of UDPB in treating wound infection**

The combination of PTT and PDT has been widely applied for combating bacterial infections (*55*, *56*). In light of the living feature to repulse pathogens through bacterial community competition, we assessed the value of Bac-MKU for treating skin wound infection caused by *S. aureus*, a clinically common pathogen that is prone to develop antibiotic resistance and leads to the emergence of various superbugs (*47*, *57*). To facilitate the evaluation of antibacterial effects, *S. aureus* was engineered to express yellow fluorescent protein (YFP) and erythromycin resistance, while Bac-MKU were prepared using Bac carrying kanamycin and ampicillin resistance, allowing the distinguishment of these bacteria by either fluorescence or bacterial counting. The assessment of the effect of irradiation duration on bacterial survival showed that the numbers of *S. aureus* treated with Bac-MK and Bac-MKU were tremendously reduced after 10-min exposure, with only sporadic bacteria remaining in the Bac-MKU group (Fig. 7, A and B). Meanwhile, the numbers of Bac-MK and Bac-MKU were also reduced (Fig. 7C). Especially, in the Bac-MKU group, bacteria were almost eliminated after 10-min irradiation, which could potentially reduce undesired side effects during in vivo application. With exposure duration extending to 15 min, all *S. aureus* in the Bac-MKU group were completely killed. However, *S. aureus* treated with Bac-MK remained a survival rate of 53.4% and Bac-MK were not fully eliminated, which, in turn, demonstrated that Bac-MKU could be used as a safe yet effective therapeutic agent for *S. aureus* infection.

Inspired by the encouraging in vitro antibacterial effects, we further evaluate the ability of Bac-MKU toward the healing of chronic wound infected with *S. aureus*. The mouse model was established by creating a skin wound with a diameter of 1.5 cm on the back and supplying with $3 \times 10^8$ CFU of *S. aureus* on the wound surface for 1 hour. After wiping, $3 \times 10^7$ CFU of Bac-MKU were added, and 4 hours later, 15-min NIR irradiation was conducted (Fig. 7E). The picture of wound to analyze the size variation at different time points was captured, and the results showed that the healing efficacy of the chronic wound in the Bac-MKU group was notably superior to those in all control groups (Fig. 7, F and G). The normalized ratio of unclosed wound size in the Bac-MKU group was near 26.7%, lower than that of the Bac-MK group 7 days after infection, whereas the chronic wound was almost healed by Bac-MKU treatment with healing time prolonging to 14 days (Fig. 7H and fig. S19). By comparison, all the PBS, Bac, and Bac-MK groups failed to achieve similar efficacy to Bac-MKU. Quantitative analysis of the remaining *S. aureus* in the wound of the Bac-MKU group exhibited a 5- to 10-fold decrement compared to those of the PBS, Bac, and Bac-MK groups (Fig. 7I and fig. S20). Note that all the Bac, Bac-MK, and Bac-MKU were completely eliminated after playing the killing effects against *S. aureus*, implying the desired safety of these living agents for healing infected wounds (fig. S21). H&E staining of the major organs from treated mice further supported the safety of these bacterial agents (fig. S22). Meanwhile, the levels of key inflammatory cytokines including TNF-α and IL-6 were decreased after treatment with Bac-MKU (Fig. 7J). H&E staining of the skin tissues appeared that 7 days after treatment, and the numbers of neutrophils and lymphocytes in the Bac-MKU group were distinctly lower than those in the control groups (Fig. 7K). After healing for 14 days, these inflammatory cells almost disappeared in the Bac-MKU group and the epidermal layers became thicker and more compact than those in the control groups. Masson's trichrome staining pointed out that an increased level of new collagen was deposited and interweaved to construct specific network structures in the Bac-MKU group. Collectively, Bac-MKU demonstrated their superiorities in inhibiting pathogenic bacteria and accelerating the recovery of chronic wounds.

To explore the potential antibacterial mechanism, we examined whether the phototherapeutic effects induced by Bac-MKU could disrupt the integrity of the outer membrane of *S. aureus* by LIVE/DEAD fluorescence staining assay. A commonly used green nucleic acid stain SYTOX Green was used to detect the bacterial membrane integrity and label dead bacteria given its inability to penetrate intact bacterial outer membrane (*58*, *59*). As expected, non–green fluorescent bacteria were detected in the *S. aureus* plus irradiation group as well as all the unirradiated groups including *S. aureus*, Bac-MK, and Bac-MKU (Fig. 7D). Differently, under irradiation, *S. aureus* treated with Bac-MK turned green, disclosing the damage of the outer membrane and the penetration of SYTOX Green. Compared to the Bac-MK–treated group that only partial *S. aureus* turned green, the majority of *S. aureus* in the Bac-MKU–treated group were stained with SYTOX Green, suggesting the destruction of the outer membranes by the synergistic photothermal and photodynamic effect. We also used SEM to observe the changes in bacterial morphology caused by bacterial membrane disruption (fig. S23). Before irradiation, *S. aureus* displayed intact and smooth outer membrane structures. Even under irradiation, the morphologies of *S. aureus* alone and *S. aureus* treated with Bac-MK remained similar to that of natural bacteria. While the surface of *S. aureus* displayed apparent pores and wrinkles after treatment with Bac-MKU plus irradiation, further verifying potency of the synergistic effect to destruct the outer membrane and cause bacterial cell death.

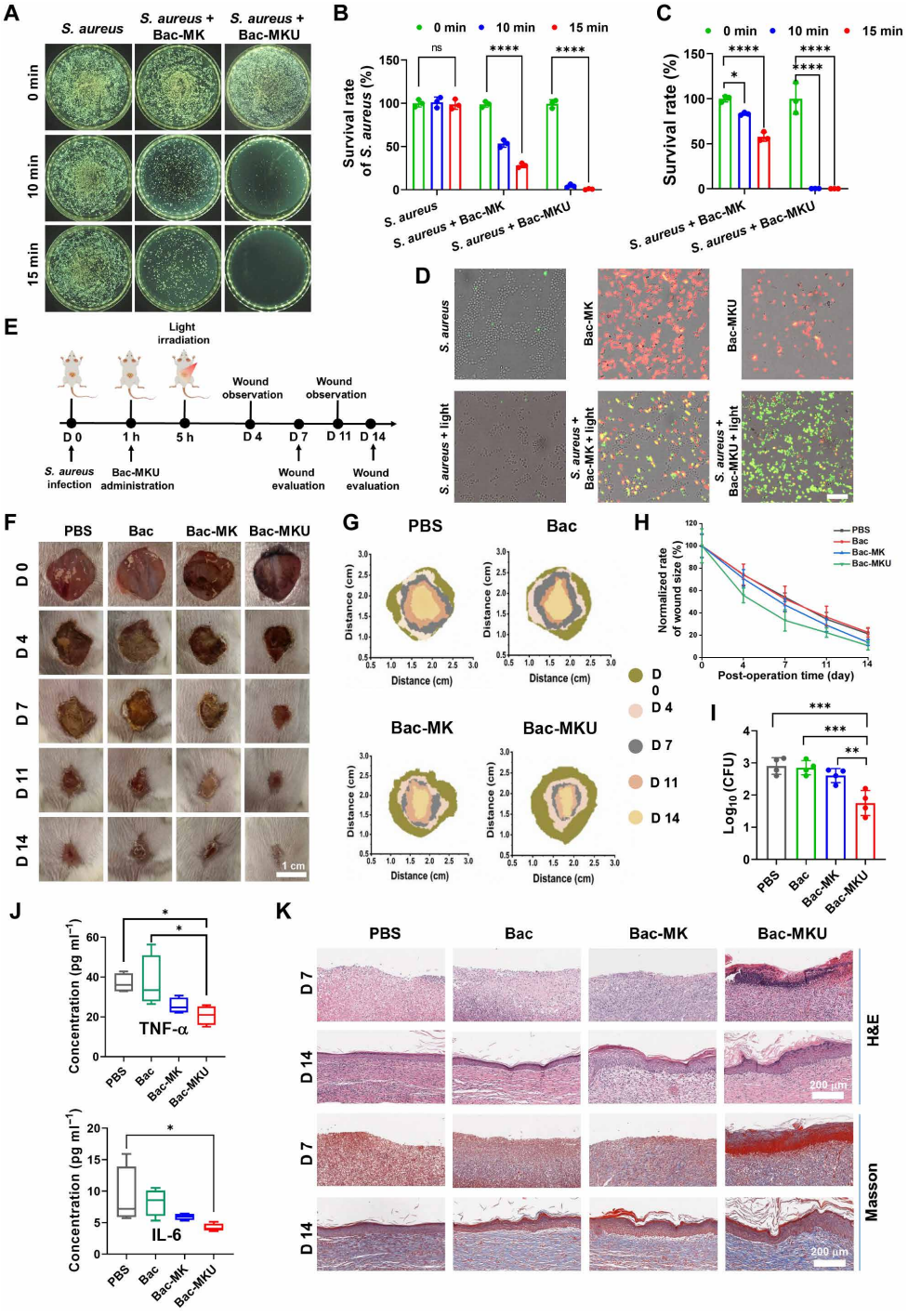


**Fig. 7. Superiorities of UDPB in treating wound infection.** (**A**) Photographs of *S. aureus* on LB agar plates supplemented with erythromycin. *S. aureus* treated with Bac-MK or Bac-MKU were irradiated under 808-nm NIR light for different durations including 0, 10, and 15 min. (**B**) Survival rates of *S. aureus* after treated with Bac-MK and Bac-MKU under 808-nm NIR light irradiation for different durations. *S. aureus* treated with PBS was used as a control. Data were presented as means ± SD ($n = 3$). (**C**) Survival rates of Bac-MK and Bac-MKU after conducting phototherapy against *S. aureus* under 808-nm NIR light irradiation for the indicated durations. Data were presented as means ± SD ($n = 3$). (**D**) Confocal images of *S. aureus* after different treatments. Scale bar, 10 μm. Samples were irradiated with 808-nm NIR light for 15 min. Bacteria were stained with SYTO Green (a green dye for dead bacteria) to distinguish from the red fluorescence of Bac-MK. (**E**) Experimental design for assessing therapeutic efficacy. (**F**) Photographs of mice wounds infected with *S. aureus* under the treatments of PBS, Bac, Bac-MK, and Bac-MKU at days 0, 3, 7, and 14. (**G**) Traces of wound closure over time after different treatments. (**H**) Healing rates of wound sizes over time after treatment. Data were presented as means ± SD ($n = 5$). (**I**) Remaining bacterial counts in local wounds at 14 days. Data were presented as means ± SD ($n = 4$). (**J**) Qualification of TNF-α and IL-6 in serum at day 14. Data were presented as means ± SD ($n = 4$). (**K**) H&E and Masson staining of wound tissues at days 7 and 14. Significance was analyzed by one-way ANOVA with Tukey's post-test. *$P < 0.05$, **$P < 0.01$, ***$P < 0.001$, and ****$P < 0.0001$. ns, not significant.

## DISCUSSION

In summary, we present the development of UDPB for NIR monochromatically excitable synergistic PTT and PDT. Meanwhile, a unique monochromatic irradiation-mediated dual-activation mode is proposed by using UDPB. To prepare UDPB, an approach integrating genetic engineering and surface modification is used. Hence, bacteria are first bioengineered to dually express photothermal melanin and photosensitive KillerRed. Then, with the help of imidoester reaction using a Traut's reagent, the primary amino residues on the surface of the engineered bacteria are converted to free sulfydryl moieties for thiol-mediated click conjugation of UCNPs. Upon NIR irradiation, the photothermal conversion of melanin can be triggered directly, while the photodynamic effect of KillerRed can be induced indirectly by the upconverted visible light emission. UDPB show inherent superiorities in combination phototherapy by virtue of their living properties that can colonize hypoxic tumor site and repulse pathogens via bacterial community competition. During in vivo assessments in mice separately developed with subcutaneous breast tumor and *S. aureus*–infected skin wound, UDPB verify appealing therapeutic values by producing adequate local hyperthermia and ROS level in the lesion sites. We find that UDPB not only provoke a potent antitumor response by eliciting a systemic immune response and causing tumor cell apoptosis but also accelerate the healing of chronic wound by damaging the outer membrane of *S. aureus* and alleviating proinflammatory reactions. Given the versatility of bioengineering to produce diverse biomolecules and the flexibility of surface modification to introduce various exogenous functional motifs, we believe that UDPB offer a universal platform for preparing next-generation phototherapeutic agents and propose a feasible approach for combining different phototherapies and beyond for disease treatment.

## MATERIALS AND METHODS

### Materials and characterizations

L-tyrosine was received from Damas. $CuSO_4$ was purchased from Aladdin. Kanamycin, ampicillin, PBS, LB, and LB agar were bought from Sangon Biotech. The ROS Assay Kit (S0033S) and annexin V–FITC Apoptosis Detection Kit were obtained from Beyotime Biotechnology. SYTO Green Dead Nucleic Acid Stain was received from ALPHABIO. 1,2-distearoyl-*sn*-glycero-3-phosphoethanolamine-*N*-[methoxy(polyethyleneglycol)-2000]-maleimide (DSPE-PEG-Mal) was purchased from MedChemExpress. Traut's reagent (molecular weight of 137.63) was received from Thermo Fisher Scientific. *S. aureus* (*S. aureus* MN8) was provided by M. Li from Shanghai Jiao Tong University.

Morphology observation was conducted by TEM (HT7700, Japan) and SEM (Hitachi-SU8230, Japan). Zeta potential was measured by DLS (Zetasizer Nano ZS, UK). UV-vis absorption and fluorescence spectra were measured by spectrophotometer (Agilent Cary 100, USA) and spectrofluorometer (HORIBA FluoroMax-4 and FLS1000, USA). OD value was obtained by BioTek Synergy H1(H1MF, USA). Confocal images were obtained by Leica TCS SP8 (German) and Nikon CSU-W1SoRa (Japan). Cell apoptosis and immune detection were analyzed by flow cytometry (BD FACSVerse, USA).

### Construction of dual melanin and KillerRed expressing bacteria

Both the KillerRed and the tyrosinase for melanin were deigned to be expressed inside of the cells. Two recombinant plasmids (pET28a-MelA and p-KillerRed) were transformed into the host bacterial strain of Bac (BL21(DE3), purchased from Sangon Biotech, China) by an electroporation system. The positive transformants were separated on Luria-Bertani (LB) agar plates that were supplemented with kanamycin and ampicillin (100 μg $ml^{-1}$). Transformants containing pET28a-MelA or p-KillerRed plasmid were also constructed by electroporating the corresponding plasmid and separated by supplementing kanamycin or ampicillin (100 μg $ml^{-1}$) on LB agar plates. The *tyrosinase* variant used in this work was original from *Rhizobium phaseoli*, which was synthesized by Sangon Biotech (*60*). The *KillerRed* was from the plasmid we purchased from domestic suppliers and used as received. The gene sequences of *tyrosinase* and *KillerRed* were shown in table S1. Bacteria-expressing melanin and KillerRed (Bac-MK) and bacteria-expressing melanin (Bac-M) were cultured in LB medium containing 1 g of L-tyrosine and 94.5 mg of $CuSO_4$ at 30°C. Bacteria-expressing KillerRed were cultured with LB medium at 37°C. Afterward, all engineered bacteria were collected and resuspended in PBS for further use. We mixed the primers for both tyrosinase and KillerRed and applied them in all PCR reactions. The primer sequences were included in table S2.

### Preparation of Bac-MKU

UCNPs (Er@Yb@Nd@Y UCNPs) were synthesized according to a previously reported method (*36*, *37*). DSPE-PEG-Mal was introduced on UCNPs by ultrasonic film hydration method to obtain maleimide-modified UCNPs. Typically, oleic acid–capped UCNPs in chloroform (10 mg $ml^{-1}$, 1 ml) and DSPE-PEG-Mal in chloroform (12.5 mg, 1 ml) were mixed in the screw-neck glass bottle. A rotary evaporator was used to dry the sample as much as possible to form the film. Then, distilled water (5 ml) was added and the sample was rapidly rotated in one direction with vigorous sonication to obtain UCNPs functionalized with maleimide groups. Excess phospholipids were purified by ultracentrifugation. Traut's reagent (50 mg $ml^{-1}$, 2 μl) was added to 1 ml of Bac-MK solution ($3 \times 10^8$ CFU) at pH 8. The mixture was rapidly stirred at room temperature to introduce thiol groups on bacterial surface. After centrifuging to remove the supernatant, 200 μl of the above UCNPs functionalized with maleimide groups was mixed with thiolated bacteria in PBS and stirred for 3 hours at room temperature, allowing for the covalent click reaction between the thiol and maleimide to form upconversion bacteria hybrid system (Bac-MKU).

### Determination of the content of surface thiol groups

We used Ellman's reagent [5,5-dithio-bis(2-nitrobenzoic acid) (DTNB)] to measure the thiol group content present on bacteria. The corresponding bacterial samples ($3 \times 10^8$ CFU $ml^{-1}$) were resuspended in PBS, and DTNB was added to the bacterial solution with a working concentration of 0.1 mM. The reaction was lasted for 2 hours at room temperature. After removing bacteria by centrifugation, 200 μl of supernatant was used for detection through a microplate reader at 412 nm. To determine the thiol group content, a standard curve was established using solutions containing progressively higher concentrations of L-cysteine hydrochloride hydrate.

### Cell culture

4T1 breast cancer cells were obtained from American Type Culture Collections (ATCCs) and cultured in DMEM medium (Gibco, USA). Cell culture mediums contained 10% FBS (Gibco, USA),

streptomycin (100 μg $ml^{-1}$), and 1% penicillin-streptomycin. Cells were incubated at 37°C in humidified 5% $CO_2$.

### Photothermal performance

The photothermal performances of bacteria were studied under 808-nm NIR irradiation (Haoliangtech, China). The temperature variations were recorded with a thermal infrared camera during 300-s irradiation. To analyze the heating effects at different power densities, the PBS solution of Bac-MKU with a concentration of $3 \times 10^8$ CFU $ml^{-1}$ was exposed at 0.8, 1.0, and 1.2 W $cm^{-2}$. The photothermal performances of different groups, including Bac, Bac-K, Bac-M, Bac-MK, and Bac-MKU with a concentration of $3 \times 10^8$ CFU $ml^{-1}$ at 1.0 W $cm^{-2}$ were recorded for comparing the rising effects. PBS was chosen as a control. Four rounds of 808-nm light irradiation at 1.0 W $cm^{-2}$ were applied to the Bac-MKU solution by turning on/off the light device to measure the photothermal stability. To test the heating effect of bacterial samples, 4T1 tumor cells were first seeded into a 96-well plate. After overnight growth, the supernatant was removed, and DMEM solutions with different groups at the final concentration of $3 \times 10^8$ CFU $ml^{-1}$ were added to each group. The samples were then irradiated by laser, and the temperature variations were recorded. To further analyze the heating effect of bacterial samples, *S. aureus* with the final concentration of $3 \times 10^8$ CFU per ml were mixed with an equal concentration of bacterial samples. PBS solution was used as a control. The samples were then irradiated by laser, and the temperature variations were recorded.

### Photodynamic performance

DCFH-DA, a commercial ROS detection kit, was used to test the photodynamic effect of bacterial materials. Before measurement, 12.5 μl of DCFH-DA was added into 0.5 ml of NaOH aqueous solution (0.01 mol $liter^{-1}$) with oscillating for 30 min in the dark. The solution was stored in an iced water bath after adding 2.5 ml of PBS. Different bacterial groups at the concentration of $3 \times 10^8$ CFU $ml^{-1}$ were irradiated under light for 1 min. The equal volume of the aforementioned working reagent was mixed with different bacterial solutions quickly. The fluorescence values at 488-nm excitation and 525-nm emission were detected by a microplate reader (TECAN Spark, Switzerland). The ROS generation inside 4T1 cells under light irradiation was investigated. 4T1 cells in the confocal dish (Thermo Fisher Scientific, USA) were incubated with DCFH-DA (final concentration of 10 μM) for 30 min in the dark. After washing with PBS for several times, different bacterial groups at the final concentration of $3 \times 10^8$ CFU $ml^{-1}$ were added to the cells and incubated for 2 hours. The samples were irradiated under NIR light for 1 min. After irradiation, the cells were observed by CLSM. The ROS generation inside *S. aureus* cells under light irradiation was also investigated. *S. aureus* cells were first incubated with DCFH-DA (final concentration of 10 μM) for 30 min in the dark, and after PBS washing for several times, the different bacterial groups at the final concentration of $3 \times 10^8$ CFU $ml^{-1}$ were added to the *S. aureus* cells. The samples were irradiated under NIR light for 1 min. The fluorescence values at 488-nm excitation and 525-nm emission were detected by a microplate reader.

### Apoptosis assay

The cell apoptosis assay against 4T1 cells was performed by flow cytometry after annexin V–FITC and PI staining. 4T1 cells, divided into six groups with the same cell number, were mixed with different bacterial groups (the final concentration of $3 \times 10^8$ CFU $ml^{-1}$) and irradiated by NIR light irradiation for 5 min. The 4T1 cells were stained with annexin V–FITC and PI for 10 min on ice and detected immediately by flow cytometry without washing.

### Preparation of tumor spheres and their interaction with bacteria

Methylcellulose was used to prepare tumor spheres using the hanging drop method. First, 6 g of sterilized methylcellulose was dissolved in 250 ml of basal medium. Then, 250 ml of medium containing twice FBS was added to the above solution. The entire mixture was mixed overnight at 4°C and centrifuged at room temperature (5000 rpm, 2 hours) to collect the upper clear liquid and prepare the methylcellulose stock solution. The above stock solution was diluted five times with normal medium, and 4T1 cells were added (final concentration of $2 \times 10^4$ cells per 20 μl). Next, 20 μl of the liquid was dropped onto the lid of a 100-mm culture dish, which was inverted and placed on a culture dish containing 10 ml of PBS. The drops were cultivated for 7 days under standard culture conditions (5% $CO_2$ at 37°C) to allow sufficient settling time. Bac-MK and Bac-MKU were added to the precultured tumor spheres at a final concentration of $3 \times 10^8$ CFU $ml^{-1}$ and incubated for 4 hours. The group without bacteria was served as a control. The interaction between the bacteria and the tumor spheres was observed using the fluorescence of Bac-MK under confocal imaging. After incubation, the tumor spheres were subjected to 5 min of light exposure to observe the destruction degree.

### Animal studies

Animal experiments were supervised under the guidelines and approved by the ethics committee of Institutional Animal Care and Use Committee of Shanghai Jiao Tong University (A2023017).

### Determination of ROS and photothermal performance invivo

A subcutaneous 4T1 tumor model was developed using female Balb/c mice (6 to 8 weeks, purchased from SPF Biotechnology) for in vivo experiments. Different groups of Bac, Bac-K, Bac-M, Bac-MK, and Bac-MKU with $3 \times 10^7$ CFU were intratumorally injected. The tumor areas were irradiated with 1.0 W $cm^{-2}$ for 5 min after 8-hour injection. The thermal imaging camera was used to record the temperature changes of different groups, reflecting the in vivo photothermal effect. After irradiation, the mice that were treated with Bac-MK, Bac-MKU, and blank groups were euthanatized, and the tumors were removed quickly. The tumor tissues were covered with optimal cutting temperature compound (OCT) (Tissue-Tek, Sakura) and frozen at −80°C. The obtained tissues were cut to obtain thin slices rapidly and incubated with DCFH-DA (100 μM) in the dark for 30 min. After washing with PBS for several times to remove the superfluous dye, the samples were further added with 4′,6-diamidino-2-phenylindole (DAPI) containing mounting medium. The fluorescent images were obtained by CLSM. A model of chronic wound healing was developed by creating wounds on the back of mice. The wounds with the same size ($d = 1.5$ cm) were exposed to *S. aureus* ($3 \times 10^9$ CFU $ml^{-1}$, 100 μl) sufficiently for 1 hour. Then, the wounds were added with different bacterial groups ($3 \times 10^7$ CFU). The PBS group was used as a control. After full exposure for 4 hours, the wound areas were irradiated with 808-nm NIR laser at 1.0 W $cm^{-2}$ for 15 min. Then, a thermal imaging camera was used to record the changes in temperature under light irradiation. To analyze the ROS generation, the wound tissues were subjected to a similar treatment as the tumor.

### In vivo biodistribution of bacteria

To investigate the in vivo biodistribution, solutions containing $3 \times 10^7$ CFU of Bac-MKU, Bac-MK, and PBS were injected into 4T1 tumor-bearing Balb/c mice and irradiated with 808-nm NIR laser at 1.0 W $cm^{-2}$ for 5 min twice ($n = 5$). At day 5, the mice were euthanized, and blood and major organs—including the heart, liver, spleen, lung, kidney, and tumors—were collected and homogenized. The mixture was diluted with PBS and plated onto LB agar plates with kanamycin and ampicillin for bacterial counting. Subcutaneous tumor-bearing mice were intratumorally injected with or without $3 \times 10^7$ CFU of Bac-MKU. After 8-hour injection, the mice were euthanized and the tumors were removed quickly. The tumor tissues were followed by covering with OCT (Tissue-Tek, Sakura) and frozen at −80°C. A DAPI-containing mounting medium was used to make the slide. Fluorescent images were collected using CLSM.

### Assessment of antitumor effect

Female Balb/c mice (6 to 8 weeks) bearing 4T1 tumors were randomly assigned into six groups after the tumors reaching ~180 $mm^3$. The mice in each group were intratumorally injected, respectively, with $3 \times 10^7$ CFU of Bac, Bac-K, Bac-M, Bac-MK, and Bac-MKU. PBS solution was injected as a control. The tumor area was irradiated twice with 808-nm NIR laser for 5 min at 8 and 24 hours after injection, respectively. The therapeutic performances on mice bearing 4T1 tumor were evaluated by measuring body weight and tumor volume in each group during the therapeutic periods. Tumor volume was calculated as $(\text{width}_{\text{tumor}})^2 \times \text{length}_{\text{tumor}} \times 0.5$. All mice were euthanized, and the tumors were collected and photographed at day 13 after treatment. To confirm the therapeutic efficacy of Bac-MKU, a histology analysis of tumor tissues was performed after treatment. Tumor tissues were removed and fixed with a 4% paraformaldehyde solution, followed by embedding in paraffin for H&E and TUNEL staining. The major organs—including the heart, liver, spleen, lung, and kidney—were also collected for H&E staining.

### In vivo evaluation of immune responses

To evaluate the antitumor immune responses, the mice after conducting a similar method of administration as the assessment of antitumor effect were euthanized at day 5 and the spleen and draining lymph nodes (DLNs) in each group were collected. The single-cell suspensions of spleen and DLNs were directly obtained by grounding completely with a syringe plunger on a cell strainer (40 μm). To measure the activation and maturation of DCs, the cells were stained with FITC-conjugated CD11c, prep/Cyanine7-conjugated CD11b, phycoerythrin (PE)–CD80, allophycocyanin (APC)–conjugated CD86, and PE/Cyanine7-conjugated MHC2 (ABclonal Technology, China). To analyze the responses of T cells, cells were stained with APC/Cyanine7-conjugated CD3, PE-conjugated CD4, and APC-conjugated CD8. After incubating on ice for 30 min, the cells were washed and fixed, followed by permeabilized with the Foxp3/Transcription Factor Fixation/Permeabilization Kit for subsequent intracellular staining. The nuclear proteins and intracellular cytokines were measured by staining with FITC-conjugated anti-Ki67 (SolA15), PE/Cyanine7-conjugated IFN-γ antibody (XMG1.2), and PE-conjugated anti-Foxp3 (MF-14). All antibodies were from BioLegend and eBioscience. The cells were washed with PBS for several times and further analyzed by flow cytometry. The mouse serum samples were also collected for analyzing IFN-γ and TNF-α by enzyme-linked immunosorbent assay (ELISA) assay (Multi Sciences, China) according to the instruction.

### Antibacterial performance

The photokilling effects of Bac-MKU and Bac-MK on eliminating *S. aureus* were tested by using YFP-producing *S. aureus* with erythromycin resistance. YFP-producing *S. aureus* was constructed according to a previously reported method (*61*). Bac-MKU and Bac-MK with a final concentration of $3 \times 10^8$ CFU $ml^{-1}$ were mixed with an equal concentration of *S. aureus*. The added equal volume of PBS was used as the control group. The mixture was irradiated for 0, 10, and 15 min under an 808-nm NIR laser at 1.0 W $cm^{-2}$. After irradiation, the bacterial mixtures were smeared into LB agar plates supplemented with erythromycin (5 μg $ml^{-1}$) or kanamycin/ampicillin (100 μg $ml^{-1}$). The survival rate was calculated by counting the corresponding numbers at 0, 10, and 15 min, respectively, with the obtained number divided by the control. The bacterial community inhibition of Bac, Bac-MK, and Bac-MKU against *S. aureus* was also tested. Bacteria were diluted to a final concentration of $1 \times 10^8$ CFU $ml^{-1}$ and placed in a 10-ml system at 37°C with shaking for 6 hours. To measure the effect of different initial bacterial concentrations at 1:10 or 10:1, the corresponding bacteria were adjusted to $1 \times 10^7$ CFU $ml^{-1}$. The subsequent experimental procedures remained unchanged.

### Exploration of antibacterial mechanism

The morphologies of bacteria with or without light irradiation were observed by SEM. The bacterial samples were fixed with 2.5% glutaraldehyde stationary liquid for 12 hours under 4°C. The dehydrated procedures were conducted by using the increasing concentration of ethanol (30, 50, 70, 80, 90, and 100%) for 15 min. To detect the bacterial viability, different bacterial cells with or without light irradiation were harvested by centrifugation and washed with PBS for several times to remove LB medium. Bacterial samples were stained with SYTO Green dye aqueous solution for 10 min. The bacterial samples were spotted on the glass slides for observation.

### In vivo assessment of wound healing

The model of chronic wound healing was built by creating wounds on the back of mice. Female Balb/c mice (6 to 8 weeks) were used for evaluating Bac-MKU antibacterial ability in vivo. Mice were randomly divided into four groups waiting to be infected with *S. aureus*. The wounds on the mice were exposed to *S. aureus* ($3 \times 10^9$ CFU $ml^{-1}$, 100 μl) sufficiently for 1 hour. The wounds with the same size ($d = 1.5$ cm) were added with PBS, Bac, Bac-MK, and Bac-MKU ($3 \times 10^7$ CFU). After full exposure for 4 hours, the wound areas were irradiated with 808-nm NIR laser at 1.0 W $cm^{-2}$ for 15 min. A thermal imaging camera was used to record the changes in temperature under light irradiation. No further light irradiation was conducted afterward. The infected wounds were observed and recorded at different intervals (days 3, 7, 11, and 14). The remained bacteria in the wound at days 7 and 14 were counted by plate counting method after grinding wound tissues. Wound tissues at days 7 and 14 were also collected and immersed into a 4% paraformaldehyde fixative solution, followed by embedding in paraffin for H&E and Masson staining. Major organs—including the heart, liver, spleen, lung, and kidney—were collected for H&E staining to evaluate the therapeutic safety. To access the biochemical indexes of inflammation, the mice were euthanized for collecting serum samples (3000 rpm, 20 min) to detect TNF-α and IL-6 by ELISA assay (Multi Sciences, China) according to the instruction.

### Statistical analysis

All statistical analyses were based on GraphPad Prism 8 and Origin 8.0 software. The experimental figures were obtained with independent experiments. The presented data were determined by one-way analysis of variance (ANOVA) or two-way ANOVA with Tukey's post-test. Error bars represent the SD. $*P < 0.05$, $**P < 0.01$, $***P < 0.001$, and $****P < 0.0001$ represented significant difference. ns represented no significance.

## Supplementary Materials

**This PDF file includes:**

Figs. S1 to S23

Tables S1 and S2

## REFERENCES AND NOTES


1. Z. Xie, T. Fan, J. An, W. Choi, Y. Duo, Y. Ge, B. Zhang, G. Nie, N. Xie, T. Zheng, Y. Chen, H. Zhang, J. S. Kim, Emerging combination strategies with phototherapy in cancer nanomedicine. *Chem. Soc. Rev.* **49**, 8065–8087 (2020).
2. S. S. Lucky, K. C. Soo, Y. Zhang, Nanoparticles in photodynamic therapy. *Chem. Rev.* **115**, 1990–2042 (2015).
3. M. Overchuk, R. A. Weersink, B. C. Wilson, G. Zheng, Photodynamic and photothermal therapies: Synergy opportunities for nanomedicine. *ACS Nano* **17**, 7979–8003 (2023).
4. W. Li, J. Yang, L. Luo, M. Jiang, B. Qin, H. Yin, C. Zhu, X. Yuan, J. Zhang, Z. Luo, Y. Du, Q. Li, Y. Lou, Y. Qiu, J. You, Targeting photodynamic and photothermal therapy to the endoplasmic reticulum enhances immunogenic cancer cell death. *Nat. Commun.* **10**, 3349 (2019).
5. M. Lan, S. Zhao, W. Liu, C.-S. Lee, W. Zhang, P. Wang, Photosensitizers for photodynamic therapy. *Adv. Healthc. Mater.* **8**, e1900132 (2019).
6. W. Fan, B. Yung, P. Huang, X. Chen, Nanotechnology for multimodal synergistic cancer therapy. *Chem. Rev.* **117**, 13566–13638 (2017).
7. S. Goel, C. A. Ferreira, F. Chen, P. A. Ellison, C. M. Siamof, T. E. Barnhart, W. Cai, Activatable hybrid nanotheranostics for tetramodal imaging and synergistic photothermal/photodynamic therapy. *Adv. Mater.* **30**, 1704367 (2018).
8. Y. Sun, Y. Zhang, Y. Gao, P. Wang, G. He, N. T. Blum, J. Lin, Q. Liu, X. Wang, P. Huang, Six birds with one stone: Versatile nanoporphyrin for single-laser-triggered synergistic phototheranostics and robust immune activation. *Adv. Mater.* **32**, e2209394 (2020).
9. J. Huo, Q. Jia, H. Huang, J. Zhang, P. Li, X. Dong, W. Huang, Emerging photothermal-derived multimodal synergistic therapy in combating bacterial infections. *Chem. Soc. Rev.* **50**, 8762–8789 (2021).
10. S. Gai, G. Yang, P. Yang, F. He, J. Lin, D. Jin, B. Xing, Recent advances in functional nanomaterials for light–triggered cancer therapy. *Nano Today* **19**, 146–187 (2018).
11. Q. Chen, C. Wang, L. Cheng, W. He, Z. Cheng, Z. Liu, Protein modified upconversion nanoparticles for imaging-guided combined photothermal and photodynamic therapy. *Biomaterials* **35**, 2915–2923 (2014).
12. W. Fan, W. Bu, J. Shi, On the latest three-stage development of nanomedicines based on upconversion nanoparticles. *Adv. Mater.* **28**, 3987–4011 (2016).
13. J. Mou, T. Lin, F. Huang, H. Chen, J. Shi, Black titania-based theranostic nanoplatform for single NIR laser induced dual-modal imaging-guided PTT/PDT. *Biomaterials* **84**, 13–24 (2016).
14. S. Wilhelm, A. J. Tavares, Q. Dai, S. Ohta, J. Audet, H. F. Dvorak, W. C. W. Chan, Analysis of nanoparticle delivery to tumours. *Nat. Rev. Mater.* **1**, 16014 (2016).
15. N. S. Forbes, Engineering the perfect (bacterial) cancer therapy. *Nat. Rev. Cancer* **10**, 785–794 (2010).
16. Y. Liu, M. Zhang, X. Wang, F. Yang, Z. Cao, L. Wang, J. Liu, Dressing bacteria with a hybrid immunoactive nanosurface to elicit dual anticancer and antiviral immunity. *Adv. Mater.* **35**, e2210949 (2023).
17. L. Wang, Z. Cao, M. Zhang, S. Lin, J. Liu, Spatiotemporally controllable distribution of combination therapeutics in solid tumors by dually modified bacteria. *Adv. Mater.* **34**, e2106669 (2022).
18. X. Wang, Z. Cao, M. Zhang, L. Meng, Z. Ming, J. Liu, Bioinspired oral delivery of gut microbiota by self-coating with biofilms. *Sci. Adv.* **6**, eabb1952 (2020).
19. J.-X. Fan, M.-T. Niu, Y.-T. Qin, Y.-X. Sun, X.-Z. Zhang, Progress of engineered bacteria for tumor therapy. *Adv. Drug Deliv. Rev.* **185**, 114296 (2022).
20. F. Wu, J. Liu, Decorated bacteria and the application in drug delivery. *Adv. Drug Deliv. Rev.* **188**, 114443 (2022).
21. C. R. Gurbatri, N. Arpaia, T. Danino, Engineering bacteria as interactive cancer therapies. *Science* **378**, 858–864 (2022).
22. Z. Ming, L. Han, M. Bao, H. Zhu, S. Qiang, S. Xue, W. Liu, Living bacterial hydrogels for accelerated infected wound healing. *Adv. Sci.* **8**, e2102545 (2021).
23. Z. Cao, S. Cheng, X. Wang, Y. Pang, J. Liu, Camouflaging bacteria by wrapping with cell membranes. *Nat. Commun.* **10**, 3452 (2019).
24. R. Sun, M. Liu, J. Lu, B. Chu, Y. Yang, B. Song, H. Wang, Y. He, Bacteria loaded with glucose polymer and photosensitive ICG silicon-nanoparticles for glioblastoma photothermal immunotherapy. *Nat. Commun.* **13**, 5127 (2022).
25. D. Zhu, J. Zhang, G. Luo, Y. Duo, B. Z. Tang, Bright bacterium for hypoxia-tolerant photodynamic therapy against orthotopic colon tumors by an interventional method. *Adv. Sci.* **8**, e2004769 (2021).
26. H. Guo, Z. Cao, J. Li, Z. Fu, S. Lin, L. Wang, J. Liu, Integrating bacteria with a ternary combination of photosensitizers for monochromatic irradiation-mediated photoacoustic imaging-guided synergistic photothermal therapy. *ACS Nano* **17**, 5059–5071 (2023).
27. X. Deng, W. Yang, Z. Shao, Y. Zhao, Genetically modified bacteria for targeted phototherapy of tumor. *Biomaterials* **272**, 120809 (2021).
28. C. Yin, Z. Wang, C. Dai, B. Yang, W. Wang, E. Yang, F. Guo, C. Fan, P. Zhang, J. Sun, D. Sun, Light-triggered photosynthetic engineered bacteria for enhanced-photodynamic therapy by relieving tumor hypoxic microenvironment. *Theranostics* **13**, 1632–1648 (2023).
29. Y. Chen, Z.-H. Li, X. Zeng, X.-Z. Zhang, Bacteria-based bioactive materials for cancer imaging and therapy. *Adv. Drug Deliv. Rev.* **193**, 114696 (2023).
30. V. Ntziachristos, A. G. Yodh, M. Schnall, B. Chance, Concurrent MRI and diffuse optical tomography of breast after indocyanine green enhancement. *Proc. Natl. Acad. Sci. U.S.A.* **97**, 2767–2772 (1999).
31. R. Weissleder, A clearer vision for in vivo imaging. *Nat. Biotechnol.* **19**, 316–317 (2001).
32. Y. Guo, Q. Sun, F.-G. Wu, Y. Dai, X. Chen, Polyphenol-containing nanoparticles: Synthesis, properties, and therapeutic delivery. *Adv. Mater.* **33**, e2007356 (2021).
33. H. Liu, Y. Yang, Y. Liu, J. Pan, J. Wang, F. Man, W. Zhang, G. Liu, Melanin-like nanomaterials for advanced biomedical applications: A versatile platform with extraordinary promise. *Adv. Sci.* **7**, 1903129 (2020).
34. M. E. Bulina, D. M. Chudakov, O. V. Britanova, Y. G. Yanushevich, D. B. Staroverov, T. V. Chepurnykh, E. M. Merzlyak, M. A. Shkrob, S. Lukyanov, K. A. Lukyanov, A genetically encoded photosensitizer. *Nat. Biotechnol.* **24**, 95–99 (2006).
35. M. E. Bulina, K. A. Lukyanov, O. V. Britanova, D. Onichtchouk, S. Lukyanov, D. M. Chudakov, Chromophore-assisted light inactivation (CALI) using the phototoxic fluorescent protein KillerRed. *Nat. Protoc.* **1**, 947–953 (2006).
36. B. Liu, Y. Chen, C. Li, F. He, Z. Hou, S. Huang, H. Zhu, X. Chen, J. Lin, Poly(acrylic acid) modification of $Nd^{3+}$-sensitized upconversion nanophosphors for highly efficient UCL imaging and ph-responsive drug delivery. *Adv. Funct. Mater.* **25**, 4717–4729 (2015).
37. B. Liu, C. Li, Z. Xie, Z. Hou, Z. Cheng, D. Jin, J. Lin, 808 nm photocontrolled UCL imaging guided chemo/photothermal synergistic therapy with single UCNPs-CuS@PAA nanocomposite. *Dalton Trans.* **45**, 13061–13069 (2016).
38. H. Luo, Y. Chen, X. Kuang, X. Wang, F. Yang, Z. Cao, L. Wang, S. Lin, F. Wu, J. Liu, Chemical reaction-mediated covalent localization of bacteria. *Nat. Commun.* **13**, 7808 (2022).
39. C. Wang, W. Sun, Y. Ye, Q. Hu, H. N. Bomba, Z. Gu, In situ activation of platelets with checkpoint inhibitors for post-surgical cancer immunotherapy. *Nat. Biomed. Eng.* **1**, 0011 (2017).
40. M. Chen, Z. Long, R. Dong, L. Wang, J. Zhang, S. Li, X. Zhao, X. Hou, H. Shao, X. Jiang, Titanium incorporation into Zr-porphyrinic metal-organic frameworks with enhanced antibacterial activity against multidrug-resistant pathogens. *Small* **16**, e1906240 (2020).
41. W. Bing, H. Sun, Z. Yan, J. Ren, X. Qu, Programmed bacteria death induced by carbon dots with different surface charge. *Small* **12**, 4713–4718 (2016).
42. K. Yang, S. Zhao, B. Li, B. Wang, M. Lan, X. Song, Low temperature photothermal therapy: Advances and perspectives. *Coord. Chem. Rev.* **454**, 214330 (2022).
43. C. Liang, J. Xie, S. Luo, C. Huang, Q. Zhang, H. Huang, P. Zhang, A highly potent ruthenium(II)-sonosensitizer and sonocatalyst for in vivo sonotherapy. *Nat. Commun.* **12**, 5001 (2021).
44. Z. Fan, B. Jiang, Q. Zhu, S. Xiang, L. Tu, Y. Yang, Q. Zhao, D. Huang, J. Han, G. Su, D. Ge, Z. Hou, Tumor-specific endogenous FeII-activated, MRI-guided self-targeting gadolinium-coordinated theranostic nanoplatforms for amplification of ros and enhanced chemodynamic chemotherapy. *ACS Appl. Mater. Interfaces* **12**, 14884–14904 (2020).
45. M. J. Ware, K. Colbert, V. Keshishian, J. Ho, S. J. Corr, S. A. Curley, B. Godin, Generation of homogenous three-dimensional pancreatic cancer cell spheroids using an improved hanging drop technique. *Tissue Eng. Part C Methods* **22**, 312–321 (2016).
46. R. Nagpal, A. Kumar, M. Kumar, P. V. Behare, S. Jain, H. Yadav, Probiotics, their health benefits and applications for developing healthier foods: A review. *FEMS Microbiol. Lett.* **334**, 1–15 (2012).
47. F. D. Lowy, *Staphylococcus aureus* Infections. *N. Engl. J. Med.* **339**, 520–532 (1998).
48. L. Lin, S. Wang, H. Deng, W. Yang, L. Rao, R. Tian, Y. Liu, G. Yu, Z. Zhou, J. Song, H.-H. Yang, Z.-Y. Chen, X. Chen, Endogenous labile iron pool-mediated free radical generation for cancer chemodynamic therapy. *J. Am. Chem. Soc.* **142**, 15320–15330 (2020).
49. M. Chen, R. Dong, J. Zhang, H. Tang, Q. Li, H. Shao, X. Jiang, Nanoscale metal–Organic frameworks that are both fluorescent and hollow for self-indicating drug delivery. *ACS Appl. Mater. Interfaces* **13**, 18554–18562 (2021).

50. Y. Liu, N. Qiu, L. Shen, Q. Liu, J. Zhang, Y.-Y. Cheng, K.-H. Lee, L. Huang, Nanocarrier-mediated immunogenic chemotherapy for triple negative breast cancer. *J. Control. Release* **323**, 431–441 (2020).
51. M. Cella, F. Sallusto, A. Lanzavecchia, Origin, maturation and antigen presenting function of dendritic cells. *Curr. Opin. Immunol.* **9**, 10–16 (1997).
52. M. Zhang, L. Wang, J. Liu, Y. Pang, Envelope virus-mimetic nanovaccines by hybridizing bioengineered cell membranes with bacterial vesicles. *iScience* **25**, 104490 (2022).
53. L. Douguet, S. J. D. Hreich, J. Benzaquen, L. Seguin, T. Juhel, X. Dezitter, C. Duranton, B. Ryffel, J. Kanellopoulos, C. Delarasse, N. Renault, C. Furman, G. Homerin, C. Féral, J. Cherfils-Vicini, R. Millet, S. Adriouch, A. Ghinet, P. Hofman, V. Vouret-Craviari, A small-molecule P2RX7 activator promotes anti-tumor immune responses and sensitizes lung tumor to immunotherapy. *Nat. Commun.* **12**, 653 (2021).
54. B. G. Kraupp, B. Ruttkay-Nedecky, H. Koudelka, K. Bukowska, W. Bursch, R. Schulte-Hermann, In situ detection of fragmented dna (tunel assay) fails to discriminate among apoptosis, necrosis, and autolytic cell death: A cautionary note. *Hepatology* **21**, 1465–1468 (1995).
55. H. Hu, H. Wang, Y. Yang, J.-F. Xu, X. Zhang, A bacteria-responsive porphyrin for adaptable photodynamic/photothermal therapy. *Angew. Chem. Int. Ed.* **61**, e202200799 (2022).
56. Y. Yang, B. Chu, J. Cheng, J. Tang, B. Song, H. Wang, Y. He, Bacteria eat nanoprobes for aggregation-enhanced imaging and killing diverse microorganisms. *Nat. Commun.* **13**, 1255 (2022).
57. I. A. Myles, S. K. Datta, Staphylococcus aureus: An introduction. *Semin. Immunopathol.* **34**, 181–184 (2012).
58. B. L. Roth, M. Poot, S. T. Yue, P. J. Millard, Bacterial viability and antibiotic susceptibility testing with SYTOX green nucleic acid stain. *Appl. Environ. Microb.* **63**, 2421–2431 (1997).
59. P. Lebaron, P. Catala, N. Parthuisot, Effectiveness of SYTOX green stain for bacterial viability assessment. *Appl. Environ. Microb.* **64**, 2697–2700 (1998).
60. N. Cabrera-Valladares, A. Martínez, S. Piñero, V. H. Lagunas-Muñoz, R. Tinoco, R. de Anda, R. Vázquez-Duhalt, F. Bolívar, G. Gosset, Expression of the *mel*A gene from *Rhizobium etli* CFN42 in *Escherichia coli* and characterization of the encoded tyrosinase. *Enzyme Microb. Tech.* **38**, 772–779 (2006).
61. J. M. Yarwood, D. J. Bartels, E. M. Volper, E. P. Greenberg, Quorum sensing in *Staphylococcus aureus* biofilms. *J. Bacteriol.* **186**, 1838–1850 (2004).



**Acknowledgments**

**Funding:** This work was financially supported by the National Key Research and Development Program of China (2021YFA0909400), the National Natural Science Foundation of China (32101218, 22305153, 82302377, 32301099, 21834007, 21934007, and 22122406), the Fundamental Research Funds for the Central Universities (2020JCPT02), the Explorer Program of the Science and Technology Commission of Shanghai Municipality (21TS1400400), the Shanghai Municipal Education Commission-Gaofeng Clinical Medicine Grant Support (20181704), and the Innovative Research Team of High-Level Local Universities in Shanghai (SHSMU-ZDCX20210900). **Author contributions:** Writing—original draft: M.C., L.W., and Z.C. Conceptualization: M.C., J.L., Q.L., Z.C., and C.F. Investigation: M.C., Q.H., L.W., M.Z., and Z.C. Writing—review and editing: M.C., J.L., L.W., Q.L., Z.C., and C.F. Methodology: M.C., Q.H., L.W., Q.L., M.Z., Z.C., Y.L., and F.Y. Resources: M.C., L.W., Q.L., Z.C., and Y.L. Funding acquisition: Q.H., J.L., Z.C., and C.F. Data curation: M.C. and L.W. Validation: M.C., Q.H., and Z.C. Supervision: J.L. and C.F. Formal analysis: M.C., L.W., Z.C., and Y.L. Software: L.W. and Z.C. Project administration: M.C., J.L., Q.L., Z.C., and C.F. Visualization: M.C. and Q.L. **Competing interests:** The authors declare that they have no other competing interests. **Data and materials availability:** All data needed to evaluate the conclusions in the paper are present in the paper and/or the Supplementary Materials.

Submitted 20 September 2023
Accepted 29 January 2024
Published 6 March 2024
10.1126/sciadv.adk9485